International Journal of Solids and Structures 262–263 (2023) 112086

Contents lists available at ScienceDirect

International Journal of Solids and Structures

journal homepage: www.elsevier.com/locate/ijsolstr

3D lattice meso-scale modelling of the effect of lateral compression on tensile fracture processes in concrete

Peter Grassl

James Watt School of Engineering, University of Glasgow, Glasgow, UK

ARTICLE INFO

Keywords:
Concrete
Fracture
Tension
Lattice
Damage
Plasticity
Multiaxial stress states

ABSTRACT

The effect of lateral compressive stresses on the cracking process in tension is rarely considered in fracture models for quasi-brittle materials such as concrete. In this study, this effect is investigated by means of a meso-scale lattice approach in which a damage-plasticity constitutive model is combined with an auto-correlated random field of strength and fracture energy. In the first part of the analyses, the lattice approach is compared with experimental results in tension and compression, which shows a good agreement between simulations and experiments. Then, cells with periodic lattices and periodic boundary conditions are loaded in two steps. Firstly, compression is applied. Next, the cell is extended in the lateral direction while keeping the compressive stress constant. It is shown that with increasing compressive stress applied, the post-peak energy dissipation in tension increases. Postprocessing of the results of the analyses reveals that this increase is due to greater frictional energy dissipation and greater number of cracks than for pure tension.

1. Introduction

For nonlinear analysis of concrete structures, it is important to include the nonlinear fracture process of concrete in tension, since it may strongly influences the load capacity of structures and is the source of a particular size effect on nominal strength (Bažant, 2002), which neither follows the strength theory nor linear elastic fracture mechanics (LEFM) (Griffith, 1921). This particular size effect is strongly dependent on the length of pre-notches as shown in two independent experimental studies (Hoover et al., 2013; Grégoire et al., 2013).

Cohesive crack models are a popular choice for this type of nonlinear analyses (Hillerborg, 1985). In these models, the response of the three-dimensional fracture process zone is idealised by a stress crack opening law applied to a crack plane. Numerically, it is often more straight-forward to model the stress-crack opening law smeared out over the element length in the form of a softening stress–strain law which is dependent on the element length (Bažant and Oh, 1983), so that the resulting stress crack opening law is mesh-independent. For direct tension, the integral of the stress crack opening law is the tensile fracture energy, which is usually considered to be a material property. Less focus has been paid on the effect of multiaxial stress states on the tensile fracture process, although it is known from experimental studies on concrete subjected to multiaxial stress states, that both strength and strain at maximum stress are very sensitive to multiaxial stress states (Kupfer et al., 1969; Mills and Zimmerman, 1970; Linse and Aschl, 1976; Imran and Pantazopoulou, 2001).

In concrete structures, lateral compressive stresses during tensile cracking are present in the case of shear failure, anchorage failure of prestressing tendons, corrosion induced cracking, and bond failure. Another example, outside the research area of concrete and concrete structures, is hydraulic fracture in rock formations, which are usually subjected to complex triaxial stress states involving combinations of high compressive and induced tensile stresses. In recent experimental studies in Nguyen et al. (2020a,b) and Bažant et al. (2022b,a), it has been reported that the fracture energy in tension is indeed influenced by compressive stresses parallel to the crack plane. Moderate compression was shown to increase the fracture energy, whereas very high compression close to the compressive strength reduces the amount of energy dissipation during tensile fracture. This effect is usually not considered in cohesive crack laws, because the stress parallel to the crack does not routinely enter these formulations. On the other hand, crack band models as proposed in Bažant and Oh (1983) can in principal capture the effect of compressive stresses parallel to the crack as long as the constitutive models are formulated accordingly. Recently, it was shown in Bažant et al. (2022b) that comprehensive constitutive models, such as the microplane model M7 (Caner and Bazant, 2013) and the damage-plasticity model CDPM2 (Grassl et al., 2013), are capable of reproducing these experimental results.

The increase in fracture energy due to moderately increasing lateral compressive stresses is intriguing, since the strength in tension is reported to decrease with increasing lateral compressive stresses.

E-mail address: peter.grassl@glasgow.ac.uk.

https://doi.org/10.1016/j.ijsolstr.2022.112086
Received 4 October 2022; Received in revised form 28 November 2022; Accepted 8 December 2022
Available online 10 December 2022

There are two possible explanations for the increase of fracture energy due to compressive stresses parallel to the crack, which are discussed in Nguyen et al. (2020a). Firstly, during tensile crack formation in quasi-brittle materials such as concrete, the crack in the matrix is bridged by aggregates, which are pulled out of the cement matrix. Due to the friction between aggregates and matrix, compressive stresses lateral to the tensile direction introduce greater resistance to pull out, which results in greater energy dissipation (Bažant, 1996). Secondly, the crack path in concrete due to direct tension is tortuous, because cracking in tension is initiated at the interfacial transition zones, which are the weak points in the meso-structure of concrete. These initial cracks are then connected by fracture of the stronger matrix. This process was studied in detail in Grassl and Jirásek (2010). If compressive stresses are present, the fracture path, i.e. the geometry of how these initial cracks connect, could be constraint, which should result in multiple parallel matrix cracks to form either instead or in addition of one tortuous localised crack. The aim of the present study is to investigate these two possible effects by performing meso-scale analyses of small concrete specimens.

Suitable numerical approaches for these meso-scale simulations are discrete approaches as reported in Schlangen and van Mier (1992), Zhang et al. (2020), Yip et al. (2005), Kang et al. (2014), Cusatis et al. (2006), Smith et al. (2014) and Eliáš et al. (2015). Recent reviews of these models can be found in Nikolić et al. (2018), Bolander et al. (2021). The technique used in the present study is 3D lattice approach related to previous work reported in Grassl and Davies (2011), Athanasiadis et al. (2018) and Aldellaa et al. (2022). It follows closely the discretisation techniques presented in Yip et al. (2005), but uses constitutive models based on combinations of damage and plasticity, similar to tensorial models proposed in Grassl and Jirásek (2006). The meso-structure of concrete, consisting of stiff and strong aggregates embedded in a soft and weak matrix, is modelled by mapping random fields generated by techniques reported in Shinozuka and Jan (1972) onto the background lattice. This technique was used before in 2D in Xenos et al. (2015).

The lattice modelling is used to reproduce uniaxial tensile and compressive results reported in Gopalaratnam and Shah (1985) and Kupfer and Gerstle (1973) to show that the model is capable of producing realistic results for concrete before it is then applied to the analysis of a periodic cell for which no experimental results are available. Cells with periodic lattices and periodic displacement boundary conditions developed in Athanasiadis et al. (2018) and Grassl and Jirásek (2010) are used to apply combinations of average tension and compression strain and stress states. The results are evaluated in the form of local dissipated energy densities of individual lattice elements, which allows for identifying changes of failure modes in the meso-structure due to presence of compression parallel to the crack plane. Furthermore, the width of the fracture process zone is investigated by roughness measures used earlier in Grassl and Antonelli (2019) and Xenos et al. (2015).

With the cells with periodic boundary conditions, only a small material volume is modelled with different constraints than in experiments on fracture of larger beams, as studied in the gap test (Nguyen et al., 2020a). Therefore, it is not expected to reproduce quantitatively the experimental results of the gap-test. Instead, the main aim of this paper is to improve the understanding of the influence of compressive stresses parallel to the crack plane on the stress-crack opening response in tension. Several new contributions are presented in this work. Firstly, a 3D lattice approach with a previously proposed damage-plasticity constitutive model is combined with an auto-correlated random field for strength and fracture energy. This new lattice meso-scale model is compared for the first time to direct tension, and uniaxial and biaxial compression experiments. Furthermore, a detailed analysis of the effect of lateral compressive stresses on the tensile fracture process is carried out.

2. Lattice model

This section describes the meso-scale lattice modelling approach which is used to simulate the fracture process zone subjected to biaxial stress states. The spatial lattice discretisation is based on sequentially placed random vertices while enforcing a minimum distance. These vertices are used for dual Delaunay and Voronoi tessellations (Yip et al., 2005). The random vertices form the nodes of the lattice element (see vertices i and j in Fig. 1a). The edges of the Delaunay tetrahedra are used for the connections of the nodes, i.e. the edges give the location of the lattice elements. The mid-cross-section of the lattice elements is obtained from the facets of the Voronoi polyhedra.

Two types of boundary treatments for the lattice generation were applied. For the comparison with experimental results, the lattice was generated by modelling boundaries of the specimen using mirrored vertices as described in Yip et al. (2005) in addition to placing vertices on the boundary with a smaller minimum distance than in the region. For the analysis of combined tension and compression, a periodic lattice with periodic boundary conditions was used as described in Athanasiadis et al. (2018) which gives the opportunity to control average stress and strain fields. In this periodic setup, lattice elements cross the boundary of the cell, so that crack patterns are not influenced by these boundaries as demonstrated in Grassl and Jirásek (2010) and Grassl and Antonelli (2019).

Each node has six degrees of freedom, namely three translations and three rotations. These nodal degrees of freedom are used to compute translational displacement jumps $\mathbf{u} = \left\{u_\mathrm{n}, u_\mathrm{p}, u_\mathrm{q}\right\}^T$ at the centroid of the mid-cross-section of the element by means of rigid body kinematics assuming that the two nodes of an element belong to two rigid polyhedra, which are determined from the Delaunay and Voronoi tessellations. The nodes are not the centroids of the polyhedra except of the special case of a centroidal Voronoi tessellation which was not applied in this study. These two polyhedra meet at the facet which forms the mid-cross-section (Fig. 1b). The centroid C of the mid-cross-section (Fig. 1b) is used to model the interaction of the two polyhedra. The translational displacement jump is transformed into strain by dividing it by the element length h. This strain is used as an input for the constitutive model to compute the stress, which is then related to the nodal forces at the nodes. The rotational jump at point C is not considered in the constitutive model.

The constitutive model in the lattice approach is a damage-plasticity approach which is capable of modelling both tensile and compressive failure (Grassl and Davies, 2011; Athanasiadis et al., 2018; Aldellaa et al., 2022). The main stress–strain law is

$$\boldsymbol{\sigma} = (1-\omega)\,\mathbf{D}_\mathrm{e}\left(\boldsymbol{\varepsilon} - \boldsymbol{\varepsilon}_\mathrm{p}\right) = (1-\omega)\,\bar{\boldsymbol{\sigma}} \tag{1}$$

Here, ω is the damage variable (ranging from 0 to 1), $\boldsymbol{D}_\mathrm{e} = \mathrm{diag}\,(E, \gamma E, \gamma E)$ is the elastic stiffness matrix, where E is the Young's modulus of the equivalent lattice material and γ is a parameter which is used to control Poisson's ratio of the continuum material. The vectors $\boldsymbol{\varepsilon} = \left(\varepsilon_\mathrm{n}, \varepsilon_\mathrm{s}, \varepsilon_\mathrm{t}\right)^T$ and $\boldsymbol{\varepsilon}_\mathrm{p} = \left(\varepsilon_\mathrm{pn}, \varepsilon_\mathrm{ps}, \varepsilon_\mathrm{pt}\right)^T$ are the total and plastic strain, respectively. Furthermore, $\boldsymbol{\sigma} = \left(\sigma_\mathrm{n}, \sigma_\mathrm{s}, \sigma_\mathrm{t}\right)^T$ and $\bar{\boldsymbol{\sigma}} = \left(\bar{\sigma}_\mathrm{n}, \bar{\sigma}_\mathrm{s}, \bar{\sigma}_\mathrm{t}\right)^T$ are the nominal and effective stress, respectively. Here subscripts s and t refer to the local coordinate system of the lattice element in Fig. 1b. The plasticity part is based on the effective stress, i.e. independent of damage. The plastic strain is determined from the plasticity part assuming small strains by combining yield function in (2), flow rule in (3), hardening law in (4), and loading and unloading conditions in (5):

$$f = F\left(\bar{\boldsymbol{\sigma}}, \kappa\right) \tag{2}$$

$$\dot{\boldsymbol{\varepsilon}}_\mathrm{p} = \dot{\lambda}\frac{\partial g}{\partial \bar{\boldsymbol{\sigma}}} \tag{3}$$

$$\dot{\kappa} = \dot{\lambda} h_\kappa \tag{4}$$

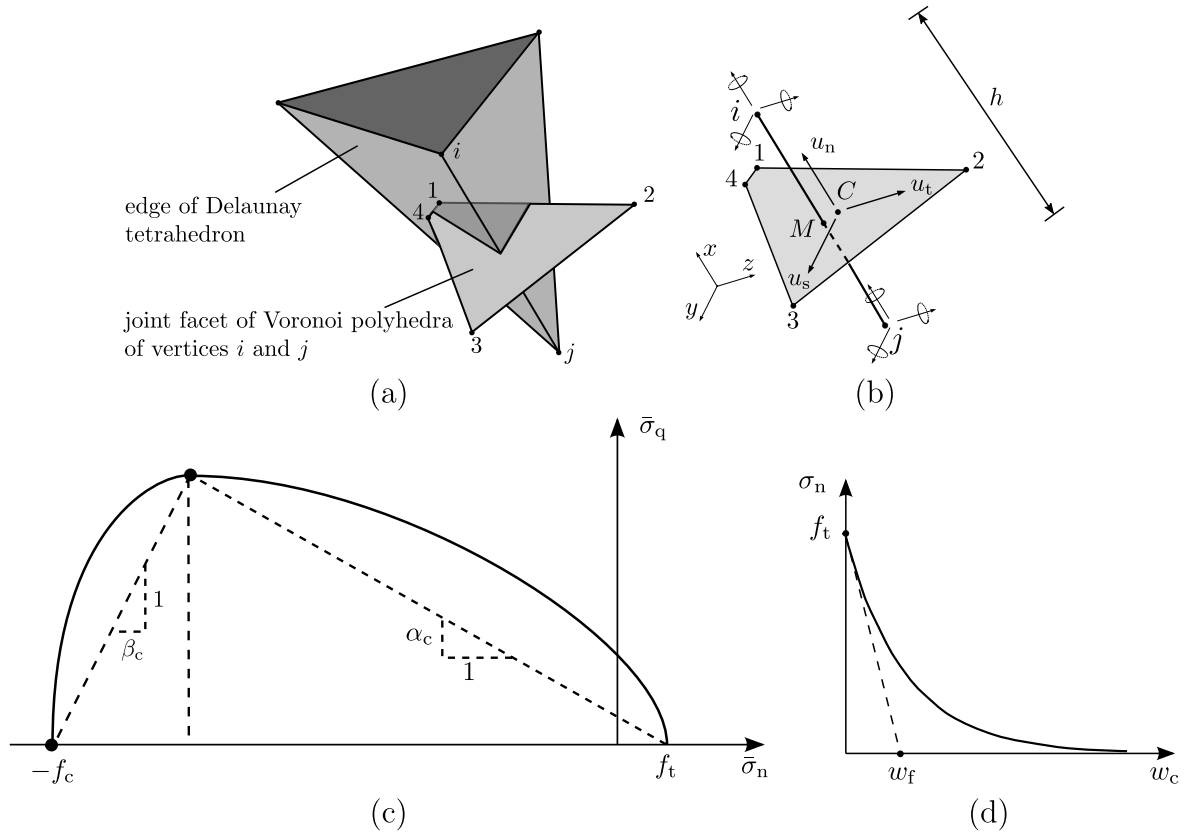

Fig. 1. Lattice model: (a) geometrical relationship between Delaunay and Voronoi tessellations, (b) lattice element with cross-section defined by the associated Voronoi facet, (c) yield surface, and (d) exponential softening law.

$$f \le 0, \qquad \dot{\lambda} \ge 0, \qquad \dot{\lambda} f = 0 \tag{5}$$

The yield function consists of two ellipsoids and has the form

$$f = \begin{cases} \alpha^2 \bar{\sigma}_n^2 - 2\alpha^2 \bar{\sigma}_n^0 \bar{\sigma}_n + \bar{\sigma}_q^2 \\ \quad - \dfrac{2\alpha^2 f_c f_t + \alpha^2 (1-\alpha\beta) f_t^2}{1+\alpha\beta} q^2 & \text{if } \bar{\sigma}_n \ge \bar{\sigma}_n^0 \\ \dfrac{\bar{\sigma}_n^2}{\beta^2} - 2\dfrac{\bar{\sigma}_n^0 \bar{\sigma}_n}{\beta^2} + \dfrac{(1-\alpha\beta) f_c^2 - 2\alpha\beta f_c f_t}{\beta^2 (1+\alpha\beta)} q^2 & \text{if } \bar{\sigma}_n < \bar{\sigma}_n^0 \end{cases} \tag{6}$$

where $\bar{\sigma}_n^0 = -\dfrac{f_c - \alpha\beta f_t}{1+\alpha\beta} q$ is the transition point of the two ellipsoids as indicated in Fig. 1c and $\bar{\sigma}_q = \sqrt{\bar{\sigma}_s^2 + \bar{\sigma}_t^2}$.

The variable q controls the hardening.

$$q = \exp\left(\frac{\kappa}{A_h}\right) \tag{7}$$

where A_h is an input parameter.

A non-associated flow rule is used, i.e. the plastic potential differs from the yield surface shown in Fig. 1c. It has the form

$$g = \begin{cases} \psi^2 \bar{\sigma}_n^2 - 2\psi^2 \bar{\sigma}_n^{0\psi} \bar{\sigma}_n + \bar{\sigma}_q^2 & \text{if } \bar{\sigma}_n \ge \bar{\sigma}_n^{0\psi} \\ \dfrac{\bar{\sigma}_n^2}{\beta^2} - 2\dfrac{\bar{\sigma}_n^{0\psi} \bar{\sigma}_n}{\beta^2 (1+\psi\beta)} + \bar{\sigma}_q^2 & \text{if } \bar{\sigma}_n < \bar{\sigma}_n^{0\psi} \end{cases} \tag{8}$$

where $\bar{\sigma}_n^{0\psi} = -\dfrac{f_c - \psi\beta f_t}{1+\psi\beta} q$ is the transition point of the two ellipsoids of the plastic potential.

The function h_κ in the evolution law in (4) is chosen as

$$h_\kappa = \left| \frac{\partial g}{\partial \sigma_n} \right| \tag{9}$$

which is the absolute value of the normal component of the direction of the plastic flow.

The damage variable ω in (1) is determined by means of the damage history variable

$$\kappa_d = \langle \varepsilon_{pn} \rangle \tag{10}$$

where $\langle . \rangle$ denotes the McAuley brackets (positive part of operator). Therefore, only positive normal plastic strain results in damage. The function of the damage variable is derived from the stress-crack opening curve in pure tension ($\sigma_n > 0$, $\sigma_q = 0$). For the damage-plasticity constitutive model, the vector of crack opening components $\mathbf{w}_c = \{w_{cn}, w_{cs}, w_{ct}\}^T$ is defined as

$$\mathbf{w}_c = h\left(\boldsymbol{\varepsilon}_p + \omega\left(\boldsymbol{\varepsilon} - \boldsymbol{\varepsilon}_p\right)\right) \tag{11}$$

For pure tension, the crack opening simplifies to

$$w_{cn} = h\left(\varepsilon_{pn} + \omega\left(\varepsilon_n - \varepsilon_{pn}\right)\right) \tag{12}$$

The stress-crack opening curve is

$$\sigma_n = f_t \exp\left(-\frac{w_{cn}}{w_f}\right) \tag{13}$$

where w_f controls the initial slope of the exponential softening curve as shown in Fig. 1d. It is related to the area under the stress-crack opening curve, i.e. fracture energy G_F, as $w_f = G_F / f_t$. For pure tension, (1) is

$$\sigma_n = (1-\omega) E \left(\varepsilon_n - \varepsilon_{pn}\right) \tag{14}$$

Setting (12) into (13), and then (13) equal to (14), a nonlinear equation of the damage variable ω is obtained, which is solved using the Newton–Raphson method.

In the lattice model, randomness of the material strength is considered by an autocorrelated random field with a Gaussian probability

function of fully correlated strength and fracture energy. The auto-correlated field has been generated with the spectral representation techniques described in Shinozuka and Jan (1972) and Shinozuka and Deodatis (1996). A square exponential function is used as the autocorrelation function.

The constitutive model requires eight input parameters. For the elastic response, the Young's modulus of the lattice material E and the shear factor γ control the macroscopic Young's modulus and Poisson's ratio. The parameters of the plasticity part are f_t, f_c, α, β, ψ and A_h. The parameter G_F (or alternatively w_f) controls the amount of energy dissipated during cracking. For the autocorrelated Gaussian field, the mean, coefficient of variation c_v and autocorrelation length l_a are required.

Postprocessing of the results is carried out in three parts. Firstly, the crack patterns are evaluated in the form of an equivalent crack width $\tilde{w}_c = \|\mathbf{w}_c\|$, where $\mathbf{w}_c$ is the crack opening vector in (12). Secondly, the energy dissipation due to fracture is computed as

$$\dot{D} = (1-\omega)\,\mathbf{D}_e\left(\boldsymbol{\varepsilon}-\boldsymbol{\varepsilon}_p\right)\dot{\boldsymbol{\varepsilon}}_p + \frac{1}{2}\left(\boldsymbol{\varepsilon}-\boldsymbol{\varepsilon}_p\right)\mathbf{D}_e\left(\boldsymbol{\varepsilon}-\boldsymbol{\varepsilon}_p\right)\dot{\omega} \tag{15}$$

More information on energy dissipation in damage-plasticity approaches can be found in Grassl (2009). To be able to distinguish between compression, shear and tensile energy dissipation, the yield surface is subdivided into three parts as shown in Fig. 2a. Based on the location on the yield surface for the current step, the energy dissipation rate is allocated to one of the three groups. The third postprocessing procedure is to evaluate the spatial variation of the fracture patterns by applying a roughness measure (Xenos et al., 2015; Grassl and Antonelli, 2019). This measure is one-dimensional and requires knowledge about the orientation of the fracture process zone. The main procedure is to calculate an average distance of all dissipated fracture processes from a reference level (see Fig. 2b) in a direction (denoted here as z) which is normal to the assumed plane of the fracture process zone. For direct tension, this direction is assumed to be equal to the one in which the load is applied. The expression is

$$\bar{z} = \sum_{i=1}^{N} w_i z_i \tag{16}$$

where w is a weight which is defined as

$$w_i = \frac{A_i \dot{D}_i}{\sum_{k=1}^{N} A_k \dot{D}_k} \tag{17}$$

The roughness measure is

$$\Delta h = \sqrt{\sum_{i=1}^{N} w_i \left(z_i - \bar{z}\right)^2} \tag{18}$$

It is the standard deviation of distance z. To illustrate the measure, consider two extreme cases. If all energy dissipation occurs on a plane with the z-axis as the normal, the roughness measure is equal to zero. On the other hand, if energy dissipation is uniformly distributed over length L in the z-direction, the roughness measure is $L/\left(2\sqrt{3}\right)$, which is the standard deviation of a uniform distribution over length L.

3. Analyses and results

The modelling approach is first applied to the analysis of two experimental studies, namely a tensile test reported in Gopalaratnam and Shah (1985) and a compression test reported in Kupfer and Gerstle (1973). After this evaluation of the capabilities of the lattice approach, the model is applied to combined tensile and compressive stresses with the periodic cell.

3.1. Comparison of meso-scale model with experiments

In this section, the lattice modelling approach is compared to two representative experiments for concrete fracture, namely a direct tensile test and uniaxial and biaxial compression experiments.

The experimental results of the tensile test modelled here were reported in Gopalaratnam and Shah (1985). The geometry of the lattice model is shown in Fig. 3a. From the experiments, it is known that the fracture processes occur in the notched region of the specimen. Therefore, only a small area around the notches was discretised with a fine lattice and random field. The input parameters for this region are $E = 50.46$ GPa, $\gamma = 0.215$, $f_t = 2.44$ MPa, $f_c = 30$ MPa, $w_f = 0.05$ mm, $A_h = 0.001$, $\alpha = 0.5$, $\psi = 0.25$, $l_a = 2.67$ mm and $c_v = 0.2$. The minimum distance between the lattice nodes is $d_{min} = 2$ mm. The input parameters are determined by inverse analysis. A uniaxial test with elastic properties is used to calibrate E and γ, so that macroscopic values for E_m and ν were obtained, which produced a good agreement with the experimental data. The lattice parameters for the nonlinear response were fitted so that the curve matches well the experimental results. For the autocorrelated field, parameters l_a and c_v were taken as proposed in Aldellaa et al. (2022) in which corrosion induced cracking was studied. For l_a, it was shown in Grassl and Jirásek (2010) and Xenos et al. (2015) that a ratio of $l_a/d_{min} = 1.333$ provided crack patterns which were independent of the lattice background mesh for 2D analyses. In this study, $l_a/d_{min} = 2.67/2 = 1.333$ was used. It should be noted that the present study does not aim to reproduce statistical size effect on strength, for which most likely a larger auto-correlation length is required as reported in Vořechovskỳ (2007) and Grassl and Bažant (2009). The effect of autocorrelation length on fracture processes was studied in detail in Eliáš and Vořechovskỳ (2020).

For the rest of the specimen, a coarser lattice was chosen with $d_{min} = 6$ mm and uniform properties equal to the mean of the random field used in the refined region. In the experiments, the end of the specimens were gripped by very stiff loading devices. In the analyses, it is assumed that these regions (hashed areas in Fig. 3a) are almost rigid (very high Young's modulus E). The notches were modelled by setting Young's modulus of elements crossing the notch planes to a very small value. The overall results of the simulations are presented in the form of the stress versus relative displacement in Fig. 3b. Here, the stress is calculated as the force divided by the ligament area of the cross-section at the height of the notches. The out-of-plane thickness of the specimen is 38 mm. The relative displacement was calculated using the vertical displacements of points E and F shown in Fig. 3a. For the analysis, an incremental-iterative approach with indirect displacement control was used. For the indirect displacement control, an equally weighted average of the relative displacements of nodes A-B, C-D and E-F were used. Three realisations of random fields, referred to random 1 to 3 in Fig. 3b, were used. Crack patterns of the analysis are shown in Fig. 4 for three stages marked in Fig. 3b for model 1. Only the notched area of the specimen is shown in which the random field was applied. The white lines indicate the notch location.

Overall, the model is capable of reproducing the experimental results well. From the stress versus notch opening curve, it can be seen that the peak stress, and strain at peak stress are well reproduced. The initial softening branch in the simulations is less steep than in the experiments, which could be due to the use of an exponential softening law instead of a bilinear one. In Jirásek and Zimmermann (1998), it was shown that a bilinear curve with strength and crack opening threshold ratios fitted can match well experimental bending results. A bilinear curve with those thresholds exhibits a steeper initial softening than a exponential softening curve with the same fracture energy. The crack patterns are reasonable as well. From the three contour plots in Fig. 4, it can be seen that two cracks initiate near the notches (because of the random field, cracks do not necessarily initiate exactly at the notch) and then meet in the centre of the specimen, which is in agreement with the experimental observations in Gopalaratnam and Shah (1985).

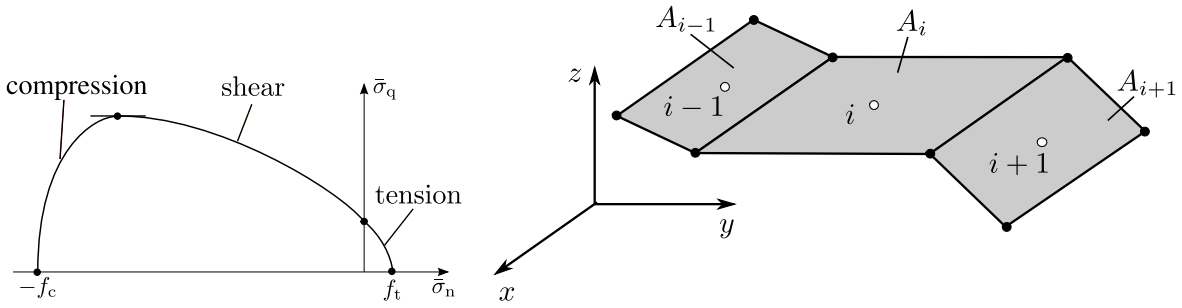

Fig. 2. Postprocessing: (a) Division of yield surface in tension, shear and compression parts. (b) Schematic illustration of segments (mid cross-sections of elements) at which energy dissipation occurs.

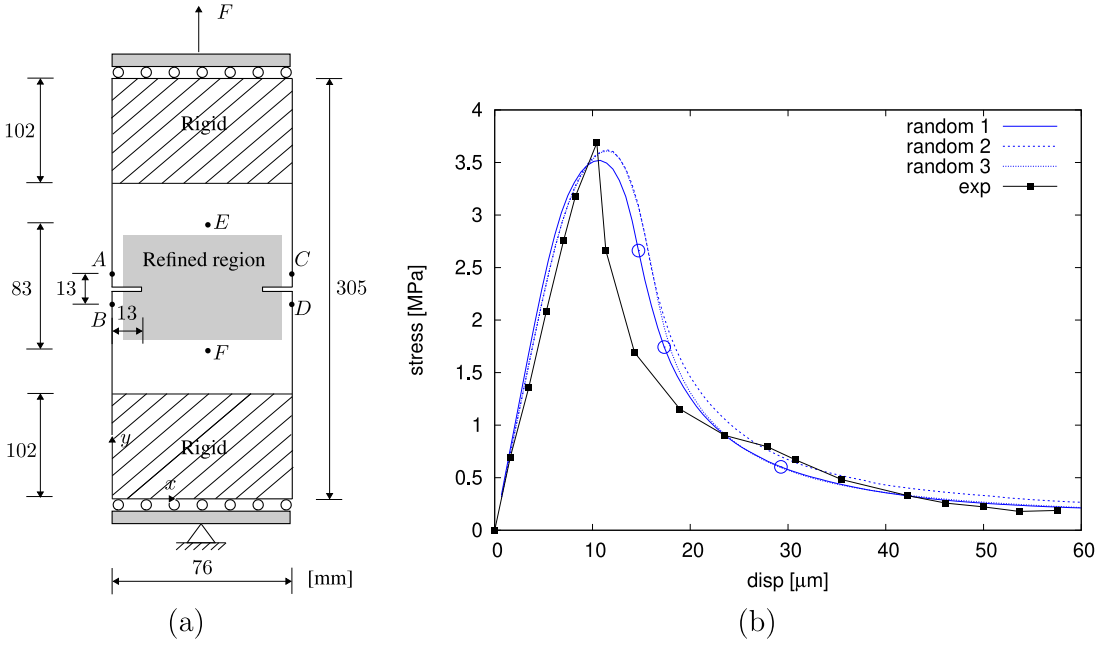

Fig. 3. (a) Geometry of the lattice specimen for the tensile test reported in Gopalaratnam and Shah (1985). The out-of plane thickness of the specimen is 38 mm. (b) Load versus crack mouth opening of the lattice simulations compared to experiments reported in Gopalaratnam and Shah (1985). The white circles mark the stages at which the crack patterns are shown in Fig. 4.

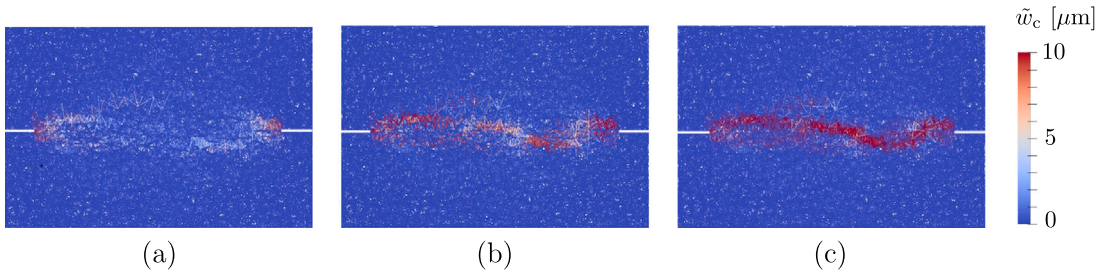

Fig. 4. Crack patterns of the direct tensile analysis. The corresponding points in the load–displacement curve are marked in Fig. 3b. Red refers to an equivalent crack width of 10 μm.

The final crack in the analysis, shown by the red region, has a width governed by the lattice element length and is tortuous which is due to the random lattice and the random field used, which was discussed in more detail previously in the 2D quantitative studies in Grassl and Jirásek (2010).

For compression, the lattice model was used to analyse uniaxial and equi-biaxial compression experiments reported in Kupfer and Gerstle (1973). The geometry and loading setup used in the simulations is shown in Fig. 5. Boundaries are assumed to be frictionless because in the experiments stiff steel brushes were used to apply the force to reduce frictional constraints. To speed up the analysis, the specimen edge length was chosen to be 100 mm in the analyses, instead of the 200 mm in the experiments. The out-of plane thickness was chosen as 10 mm. This change of the geometry is acceptable, because the failure processes for the range of displacement investigated here are distributed. The incremental-iterative approach used for the previous tensile test exhibits convergence problems when it is applied to the compression test. These problems occur close to the peak load. Therefore, the analysis is

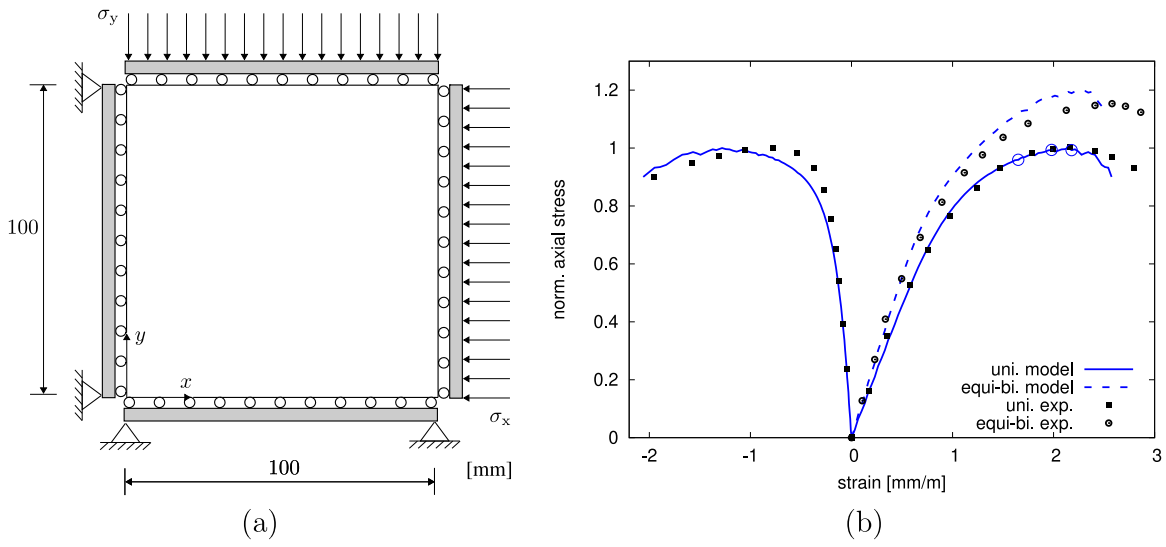

Fig. 5. (a) Geometry of the lattice specimen for the compression test reported in Kupfer and Gerstle (1973). The out-of-plane thickness is 10 mm. (b) Stress versus strain of the lattice simulations compared to experiments reported in Kupfer and Gerstle (1973). The white circles mark the stages at which the crack patterns are shown.

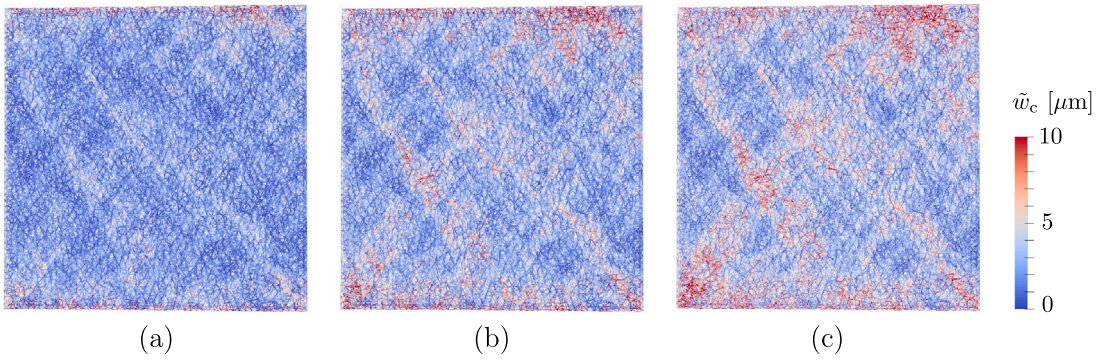

Fig. 6. Crack patterns for the uniaxial compression analysis at stages marked in the stress–strain curve in Fig. 5b.

carried out using an explicit solver and direct displacement control. A very small displacement rate is used to obtain results which are close to the quasi-static response. The input parameters are $E = 45.91$ GPa, $\gamma = 0.297$, $f_t = 3.$ MPa, $f_c = 30$ MPa, $w_f = 0.02$ mm, $A_h = 0.001$, $\alpha = 0.5$, $\psi = 0.25$, $l_a = 2.67$ mm and $c_v = 0.2$. The minimum distance between nodes is $d_{min} = 2$ mm. The results are shown in the form of stress–strain curves in Fig. 5b. For uniaxial compression, both the axial compressive and lateral tensile strain are shown. For equi-biaxial compression, the two strain components are equal. The strain in the out-of plane direction was not evaluated from the analysis, because of the small out-of-plane thickness of the specimen. In compression, the effect of the randomness on the stress–strain curve is very small. Therefore, the results of only one analysis are shown. This small effect of randomness is explained by the averaging of many nonlinear processes in the specimen. For the direct tensile test, a bigger scatter in the stress-crack opening is obtained, because the nonlinear processes are confined in a small region close to the notches. The crack patterns are shown in Fig. 6 for the uniaxial compression case for three stages marked in Fig. 5b.

The stress–strain curves are overall in good agreement with the experimental results. For the uniaxial test, both the axial as well as the lateral strain responses are well reproduced. The lattice model captures well the pre-peak nonlinearity in the axial direction. The associated lateral strain in the model is greater than in the experiments. However, this difference is small considering how difficult it is to predict and measure the lateral strain in unconfined compression. For equibiaxial compression, the model overestimates the strength obtained in the experiments. Furthermore, the strain at peak is slightly underestimated. Still, the shapes of the curves from analyses and experiments are very similar. From the crack patterns in Fig. 6 it can be seen that the cracks initiate at the boundary and are then distributed across the specimen in the form of shear bands. No splitting cracks are visible which is normally associated with compression tests without friction at the boundary. The concentration of cracks at the boundary might be due to the way the lattice is generated. Vertices are first placed on the boundary and then within the specimen. This results in a layer of lattice elements next to the boundary, which are longer than elements within the specimen.

Overall, the comparison of the lattice results with experiments for the tensile and compression test demonstrates that the lattice model is capable of reproducing the failure process of concrete. In the next step, the model is applied to investigate nonproportional loading in the form of compression and lateral tension.

3.2. *Prediction of effect of lateral compression stress on the fracture process in tension*

In this section, the lattice model is applied to investigate the effect of lateral compression on the tensile fracture process. This part of the work is motivated by the recent gap tests reported in Nguyen et al. (2020a,b) and Bažant et al. (2022b,a). In these experiments, the centre area of beams were loaded in compression by means of special support pads which yield in compression under constant force. With this constant compressive force present, bending was applied which fractured the ligament area of the notched beams in tension with the

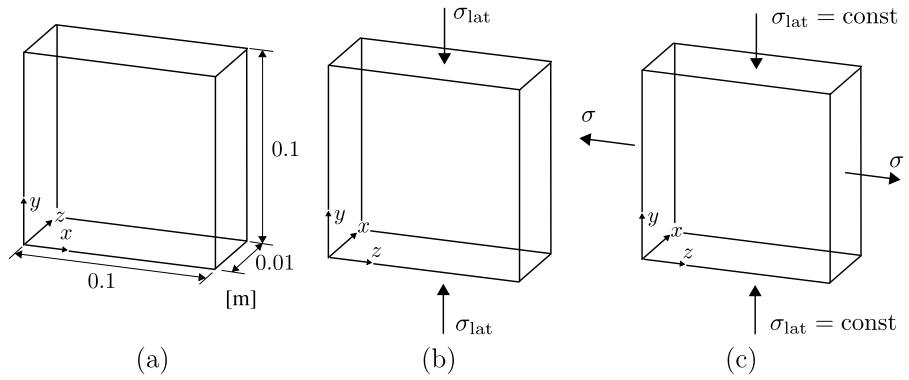

Fig. 7. FPZ: (a) Geometry of the periodic cell, (b) First load step at which compressive stress is applied. (c) Second load step with constant lateral compressive stress.

lateral compressive stresses present. It was found that fracture energy in tension increases with increasing lateral compressive stress applied.

In the present study, this nonproportional loading scenario is investigated simplified by means of a numerical cell with both periodic boundary conditions and periodic lattice structure. The periodicity of the lattice is achieved by letting lattice elements cross the boundary of the cell and connecting the degrees of freedom of these lattice elements on each side of the specimen to the average strain fields applied to the periodic cell. The details of this approach are presented in Grassl and Jirásek (2010) and Athanasiadis et al. (2018). As a result of this periodic lattice generation, tensile cracks are initiated independently of the cell's boundaries and are even free to cross boundaries as was demonstrated in Grassl and Jirásek (2010). It should be noted that the use of periodicity of the displacements introduces constraints on the crack evolution. However, these constraints are related to the direction in which the periodicity of boundary conditions is applied and not the lattice arrangement at the boundaries of the specimen. The geometry of the periodic cell is shown in Fig. 7a. The input parameters are $E = 50.46$ GPa, $\gamma = 0.215$, $f_t = 1.92$ MPa, $f_c = 30$ MPa, $w_f = 0.025$ mm, $A_h = 0.001$, $\alpha = 0.5$, $\psi = 0.25$, $l_a = 2.67$ mm and $c_v = 0.2$. These parameters are chosen so that the average tensile strength is $\bar{f}_t = 3$ MPa. The minimum distance between nodes is again $d_{\min} = 2$ mm, as before. An implicit incremental-iterative approach was used to control the analysis. The two step loading procedure is schematically shown in Fig. 7b and c. Firstly, an average compressive stress in y-direction is applied in increments until the desired value σ_{lat} is reached (Fig. 7b). Then, in the second step, the compressive stress σ_{lat} is kept constant and an average tensile strain in the z-direction is applied in increments until the specimen is completely fractured (Fig. 7c). These average stress and strain components are controlled independently using a previously proposed implementation of the boundary periodicity of the cell. Six loading schemes are analysed, which differ by the amount of lateral compressive stress σ_{lat} applied, which are $\sigma_{\text{lat}}/\bar{f}_t = 0, 2, 4, 6, 7, 8$. For each loading scheme, 10 analyses with random fields are carried out.

For $\sigma_{\text{lat}}/\bar{f}_t = 0$, the effect of randomness on the tensile response is demonstrated in Fig. 8a by showing the mean curve with error bars which represent plus/minus one standard deviation. Furthermore, the random fields for tensile strength and crack patterns for two analyses are shown in Fig. 8b. Compressive strength and fracture energy are fully correlated with tensile strength. From the results, it can be seen that the standard deviation in the pre-peak regime is very small. Only in the post-peak regime, when the strain profiles are localised in narrow zones, a bigger standard deviation is visible. This standard deviation is due to random material properties and random lattice arrangement as shown in Fig. 8b. It can be seen that due to the periodic boundary conditions and periodic lattice, there is no preferential location of the crack within the specimen. However, periodicity of the displacements requires that the localised crack reaches the boundary of the cell at the same z-coordinate value on both sides, since the cell represents only a small portion of the crack. This introduces different constraints on the crack formation, than in full size test specimens in experiments. In Grassl and Jirásek (2010), it was shown that the effect of the length of the periodic cell on the load–displacement curve is small for 2D analyses.

The results of the stress–strain curve for the prescribed displacement in the x-direction (Fig. 7) for different lateral stress levels is shown Fig. 9a as a mean of 10 analyses. The error bars representing the standard deviations, which are very similar to those presented in Fig. 8a, are not included in the graph for clarity. Furthermore, the cumulative dissipated energy is shown in 9b as a mean of 10b analyses. The total dissipated energy in the post-peak regime computed according to (15) is split in tensile, shear and compression components and the evolution of each component is shown separately as well. Furthermore, the roughness of the fracture patterns computed according to (18) is shown in Fig. 10a as mean of 10 analyses. In addition, the crack patterns for selected levels of σ_{lat} are shown in Fig. 10b. These cracks are for one of the 10 analyses for each lateral compressive stress levels at a large value of the strain. The random field for the analyses used to show the crack patterns, is the same but the level of lateral compressive stress differs.

From the stress versus strain curves in Fig. 9a, a strong effect of the lateral compressive stress σ_{lat} on strength and ductility is visible. For $\sigma_{\text{lat}}/\bar{f}_t = 2$, a small increase in the peak stress and pre-peak nonlinear is observed. This increase could be explained by the frictional-cohesive nature of concrete. Low parallel compressive stresses could increase the tensile strength as long as compression does not induce tensile damage. However, there are no experimental results available to confirm this slight increase for this specific loading procedure. For larger $\sigma_{\text{lat}}/\bar{f}_t$ values, the peak stress decreases and the pre-peak nonlinearities strongly increase. For the post-peak branch of the curve, there is only a small difference between $\sigma_{\text{lat}}/\bar{f}_t = 0$ and $\sigma_{\text{lat}}/\bar{f}_t = 2$. For larger $\sigma_{\text{lat}}/\bar{f}_t$ values, the ductility in the post-peak regime increases significantly. The decrease of the tensile strength with increasing lateral compressive stress agrees with the well documented strength envelope of concrete subjected to biaxial stress states (Kupfer and Gerstle, 1973). The change of the pre-peak and post-peak nonlinearities is less well discussed in the literature and requires further explanation. The dissipated energy of the post-peak part of the curves in Fig. 9b shows that for $\sigma_{\text{lat}}/\bar{f}_t \leq 4$ almost all of the post-peak energy dissipation occurs in tension and is not strongly affected by lateral compression. However, for greater lateral compressive stress, the shear and compression parts of energy dissipation increase more than the tensile part. This indicates that for large lateral compressive stresses, friction is activated which constitutes another form of energy dissipation in addition to the tensile dissipation. This observation is related to Bažant (1996) where it was shown that the energy dissipation during tensile fracture is also due plastic-frictional energy dissipation. In this study, the chosen division in tensile, shear and compressive energy (Fig. 2) is rather arbitrary and it could be argued that the tensile energy dissipation contains also dissipation in shear. Still, the increase of the shear and compression dissipation

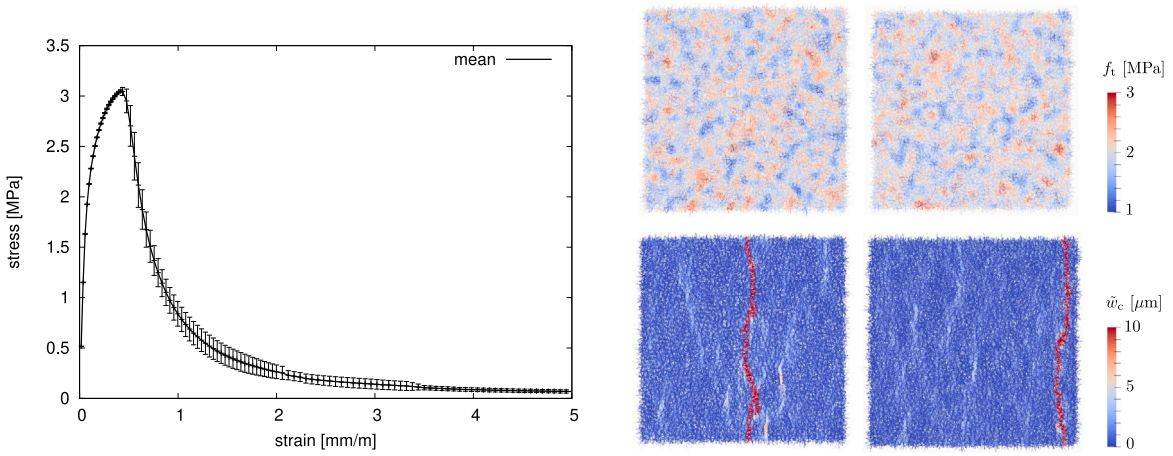

Fig. 8. FPZ:(a) Average stress versus average strain in x-direction for $\sigma_{lat}/\bar{f}_t = 0$. The error bars show plus/minus one standard deviation based on 10 random analyses. (b) Examples of random fields of tensile strength (top) and crack patterns (bottom) of two analyses for $\sigma_{lat}/\bar{f}_t = 0$.

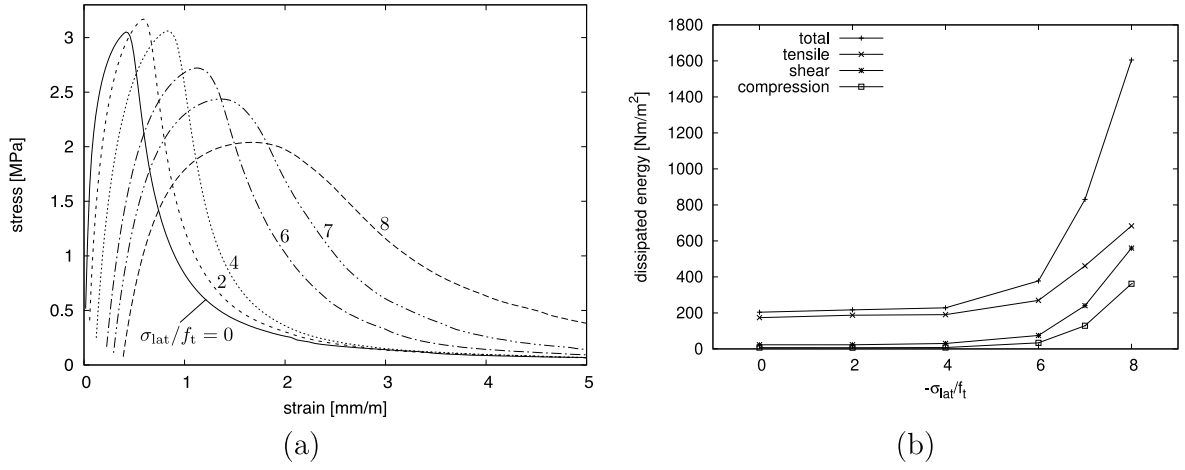

Fig. 9. FPZ: (a) Average stress versus strain in x-direction for varying lateral compressive stress. (b) Dissipated energy versus lateral compressive stress.

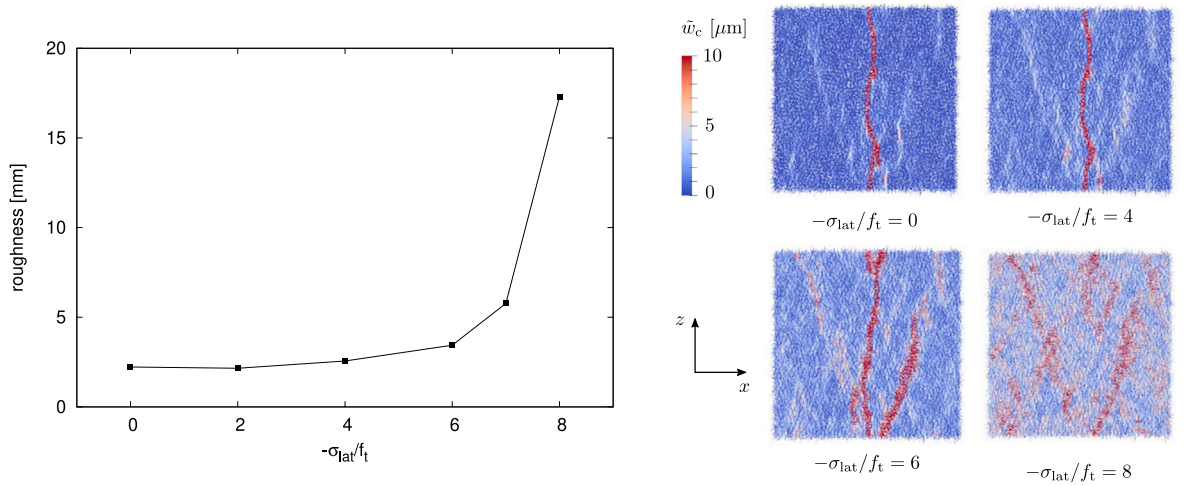

Fig. 10. FPZ: (a) Roughness measure versus lateral compressive stress. (b) Fracture patterns for varying lateral stresses in the z-direction σ_{lat} in the z-direction.

with larger lateral compressive stresses indicates that friction plays a role in the energy dissipation.

The total increase in dissipation is not only explained by the activation of friction, as can be seen by the increase of tensile dissipation. The additional energy dissipation in tension can be explained by the increase in the number of cracks with increasing lateral compressive stress as shown in Fig. 10b. These crack patterns are for one random field. A representation in the form of mean values is shown in Fig. 10a in the form of the roughness measure. The more cracks there are in the specimen, the greater is the roughness measure defined in (18). At the lateral stress level at which the tensile energy dissipation increases the roughness measure increases as well. Therefore, the increase in tensile energy dissipation is due to the formation of multiple tensile cracks. The reason for these additional cracks is found by studying the tortuosity of tensile cracking in concrete. If the crack path is perfectly straight, lateral compressive stress would not initiate additional tensile cracks. However, from the results for $\sigma_{\text{lat}}/\bar{f}_{\text{t}} \leq 0$ in Fig. 8b, it can be seen that the localised crack in tension is tortuous. The cracking process starts at weak locations off the centre line of the crack plane, which are then connected by inclined crack segments to form one localised crack. If large compressive stresses are present, the formation of these connecting segments is initially suppressed and other crack directions in which energy is dissipated in tension are created. Only at a later stage the crack localises. It is also important to point out that the lateral compressive stress is applied as a multiple of the tensile strength, which stays constant during the tensile fracture process. Therefore, during the cracking process, when the average tensile stress decreases, the ratio of lateral compressive stress versus tensile stress increases.

4. Conclusions

From the analyses of tensile fracture with lateral compression with the proposed meso-scale lattice approach a number of conclusions are drawn. The proposed lattice approach is capable of reproducing the response of concrete in tension, uniaxial and biaxial compression as the comparison with experimental results has shown. The lattice model predicts that large lateral compressive stresses decrease the tensile strength, which is in agreement with experimental results. The presence of lateral compressive stresses increase post-peak energy dissipation. For the range of lateral stresses considered, the greater the lateral stress is, the greater is the post-peak energy dissipation. The postprocessing, based on dissipated energy and roughness measures, shows that the increase in post-peak dissipation is due activation of friction and widening of the fracture process zone. From the crack patterns, it can be seen that the spatially correlated random fields result in a tortuous crack path from which, if parallel compressive stresses are present, additional inclined cracks are induced.

Declaration of competing interest

The authors declare that they have no known competing financial interests or personal relationships that could have appeared to influence the work reported in this paper.

Data availability

Data will be made available on request.

Acknowledgements

The lattice simulations were carried out with the finite element programme OOFEM (Patzák, 2012) modified by the author.

References

Aldellaa, I., Havlásek, P., Jirásek, M., Grassl, P., 2022. Effect of creep on corrosion-induced cracking. Eng. Fract. Mech. 264, 108310.
Athanasiadis, I., Wheeler, S.J., Grassl, P., 2018. Hydro-mechanical network modelling of particulate composites. Int. J. Solids Struct. 130–131, 49–60.
Bažant, Z.P., 1996. Analysis of work-of-fracture method for measuring fracture energy of concrete. J. Eng. Mech. 122 (2), 138–144.
Bažant, Z.P., 2002. Scaling of Structural Strength. Hermes-Penton, London.
Bažant, Z.P., Dönmez, A.A., Nguyen, H.T., 2022a. Précis of gap test results requiring reappraisal of line crack and phase-field models of fracture mechanics. Eng. Struct. 250, 113285.
Bažant, Z.P., Nguyen, H.T., Dönmez, A.A., 2022b. Critical comparison of phase-field, peridynamics and crack band model M7 in light of gap test and classical fracture tests. J. Appl. Mech. 1–79.
Bažant, Z.P., Oh, B.-H., 1983. Crack band theory for fracture of concrete. Mater. Struct. 16, 155–177.
Bolander, J.E., Eliáš, J., Cusatis, G., Nagai, K., 2021. Discrete mechanical models of concrete fracture. Eng. Fract. Mech. 257, 108030.
Caner, F.C., Bazant, Z.P., 2013. Microplane model M7 for plain concrete. I: Formulation. Mechanics 139 (12).
Cusatis, G., Bažant, Z.P., Cedolin, L., 2006. Confinement-shear lattice CSL mode for fracture propagation in concrete. Comput. Methods Appl. Mech. Engrg. 195, 7154–7171.
Eliáš, Jan, Vořechovskỳ, Miroslav, 2020. Fracture in random quasibrittle media: I. discrete mesoscale simulations of load capacity and fracture process zone. Eng. Fract. Mech. 235, 107160.
Eliáš, J., Vořechovský, M., Skoček, J., Bažant, Z.P., 2015. Stochastic discrete meso-scale simulations of concrete fracture: comparison to experimental data. Eng. Fract. Mech..
Gopalaratnam, V.S., Shah, S.P., 1985. Softening response of plain concrete in direct tension. ACI J. Proc. 82 (3).
Grassl, P., 2009. On a damage-plasticity approach to model concrete failure. Proc. ICE - Eng. Comput. Mech. 162, 221–231.
Grassl, P., Antonelli, A., 2019. 3D network modelling of fracture processes in fibre-reinforced geomaterials. Int. J. Solids Struct. 156–157, 234–242.
Grassl, P., Bažant, Z.P., 2009. Random lattice-particle simulation of statistical size effect in quasi-brittle structures failing at crack initiation. J. Eng. Mech. 135, 85–92.
Grassl, P., Davies, T., 2011. Lattice modelling of corrosion induced cracking and bond in reinforced concrete. Cem. Concr. Compos. 33, 918–924.
Grassl, P., Jirásek, M., 2006. Damage-plastic model for concrete failure. Int. J. Solids Struct. 43, 7166–7196.
Grassl, P., Jirásek, M., 2010. Meso-scale approach to modelling the fracture process zone of concrete subjected to uniaxial tension. Int. J. Solids Struct. 47, 957–968.
Grassl, P., Xenos, D., Nyström, U., Rempling, R., Gylltoft, K., 2013. CDPM2: A damage-plasticity approach to modelling the failure of concrete. Int. J. Solids Struct. 50 (24), 3805–3816.
Grégoire, D., Rojas-Solano, L.B., Pijaudier-Cabot, G., 2013. Failure and size effect for notched and unnotched concrete beams. Int. J. Numer. Anal. Methods Geomech. 37 (10), 1434–1452.
Griffith, A.A., 1921. The phenomena of rupture and flow in solids. Philos. Trans. R. Soc. Lond. Ser. A 221, 163–197.
Hillerborg, A., 1985. The theoretical basis of a method to determine the fracture energy G_F of concrete. Mater. Struct. 18 (4), 291–296.
Hoover, C., Bažant, Z.P., Vorel, J., Wendner, R., Hubler, M., 2013. Comprehensive concrete fracture tests: Description and results. Eng. Fract. Mech. 114, 92–103.
Imran, I., Pantazopoulou, S.J., 2001. Plasticity model for concrete under triaxial compression. ASCE J. Eng. Mech. 127, 281–290.
Jirásek, M., Zimmermann, T., 1998. Rotating crack model with transition to scalar damage. J. Eng. Mech. 124, 277–284.
Kang, J., Kim, K., Lim, Y.M., Bolander, J.E., 2014. Modeling of fiber-reinforced cement composites: Discrete representation of fiber pullout. Int. J. Solids Struct. 51 (10), 1970–1979.
Kupfer, H.B., Gerstle, K.H., 1973. Behavior of concrete under biaxial stresses. J. Eng. Mech. ASCED 99, 853–866.
Kupfer, H., Hilsdorf, H.K., Rüsch, H., 1969. Behavior of concrete under biaxial stresses. J. Am. Concr. Inst. 66, 656–666.
Linse, D., Aschl, H., 1976. Versuche zum Verhalten von Beton unter Mehrachsiger Banspruchung. Versuchsbericht. Technical University München.
Mills, L.L., Zimmerman, R.M., 1970. Compressive strength of plain concete under multiaxial loading conditions. ACI J. 67, 802–807.
Nguyen, H.T., Pathirage, M., Cusatis, G., Bažant, Z.P., 2020b. Gap test of crack-parallel stress effect on quasibrittle fracture and its consequences. J. Appl. Mech. 87 (7), 071012.
Nguyen, H., Pathirage, M., Rezaei, M., Issa, M., Cusatis, G., Bažant, Z.P., 2020a. New perspective of fracture mechanics inspired by gap test with crack-parallel compression. Proc. Natl. Acad. Sci. 117 (25), 14015–14020.
Nikolić, M., Karavelić, E., Ibrahimbegovic, A., Miščević, P., 2018. Lattice element models and their peculiarities. Arch. Comput. Methods Eng. 25 (3), 753–784.

Patzák, B., 2012. OOFEM – An object-oriented simulation tool for advanced modeling of materials and structure. Acta Polytech. 52, 59–66.
Schlangen, E., van Mier, J.G.M., 1992. Simple lattice model for numerical simulation of fracture of concrete materials and structures. Mater. Struct. 25, 534–542.
Shinozuka, M., Deodatis, G., 1996. Simulation of multi-dimensional gaussian stochastic fields by spectral representation. Appl. Mech. Rev. ASME 49, 29–53.
Shinozuka, M., Jan, C.-M., 1972. Digital simulation of random processes and its applications. J. Sound Vib. 25, 111–128.
Smith, J., Cusatis, G., Pelessone, D., Landis, E., O'Daniel, J., Baylot, J., 2014. Discrete modeling of ultra-high-performance concrete with application to projectile penetration. Int. J. Impact Eng. 65, 13–32.
Vořechovskỳ, M., 2007. Interplay of size effects in concrete specimens under tension studied via computational stochastic fracture mechanics. Int. J. Solids Struct. 44 (9), 2715–2731.
Xenos, D., Grégoire, D., Morel, S., Grassl, P., 2015. Calibration of nonlocal models for tensile fracture in quasi-brittle heterogeneous materials. J. Mech. Phys. Solids 82, 48–60.
Yip, M., Mohle, J., Bolander, J.E., 2005. Automated Modeling of Three-Dimensional Structural Components Using Irregular Lattices. Comput.-Aided Civ. Infrastruct. Eng. 20 (6), 393–407.
Zhang, H., Xu, Y., Gan, Y., Schlangen, E., Šavija, B., 2020. Experimentally validated meso-scale fracture modelling of mortar using output from micromechanical models. Cem. Concr. Compos. 110, 103567.